

Exploring tidal effects of coalescing binary neutron stars in numerical relativity

Kenta Hotokezaka,¹ Koutarou Kyutoku,² and Masaru Shibata³

¹*Department of Physics, Kyoto University, Kyoto 606-8502, Japan*

²*Theory Center, Institute of Particles and Nuclear Studies, KEK, Tsukuba, 305-0801, Japan*

³*Yukawa Institute for Theoretical Physics, Kyoto University, Kyoto 606-8502, Japan*

We study gravitational waves emitted in the late inspiral stage of binary neutron stars by analyzing the waveform obtained in numerical-relativity simulations. For deriving the physical gravitational waveforms from the numerical results, the resolution extrapolation plays an essential role for our simulations. The extrapolated gravitational-wave phases are compared with those calculated in the post-Newtonian (PN) and effective-one-body (EOB) formalisms including corrections of tidal effects. We show that the extrapolated gravitational-wave phases in numerical relativity agree well with those by the PN and EOB calculations for most of the inspiral stage except for a tidally-dominated, final inspiral stage, in which the PN and EOB results underestimate the tidal effects. Nevertheless, the accumulated phase difference between our extrapolated results and the results by the PN/EOB calculations is at most 1–3 radian in the last 15 cycles.

PACS numbers: 04.25.D-, 04.30.Db

I. INTRODUCTION

The inspiral and merger of coalescing compact binaries are among the most promising sources for kilometer-size laser-interferometric gravitational-wave detectors [1–3]. A statistical study based on the stellar evolution synthesis (e.g., Refs. [4, 5]) suggests that detection rate $\sim 1 - 100 \text{ yr}^{-1}$ may be achieved by advanced detectors such as advanced LIGO [6], advanced VIRGO [7], and KAGRA (LCGT) [8], which will be in operation in this decade.

One of the key goals after the first detection of gravitational waves from inspiraling black hole-neutron star (BH-NS) binaries and binary neutron stars (NS-NS) achieved in the near future will be to extract binary parameters such as mass, spin, and radius of each object in the binary systems. In particular, the mass and quantities related to the finite size of the neutron star will provide us the essential information for the equation of state (EOS) of the neutron-star matter. The mass of two neutron stars will be determined with a high accuracy $\lesssim 1\%$, if the gravitational-wave signals in the inspiral stage are detected with the signal-to-noise ratio $\gtrsim 10$ [9].

It is more challenging to determine the parameters related to the finite size of neutron stars. Several methods to measure such a quantity by observing the gravitational-wave signals from NS-NS and BH-NS binaries have been already proposed [10–17]. In particular, extracting the tidal deformability of neutron stars from the gravitational-wave signals from NS-NS inspirals is one of the convincing ways [21]. For realizing this method, one needs to go beyond the point-particle approximation to model the gravitational waveform in NS-NS inspirals. In other words, one has to derive the gravitational waveform in NS-NS inspirals including tidal effects, which influence the dynamics of the binary systems in the late inspiral phase (e.g., Ref. [18]). When the tidal deformability of a neutron star can be measured by the gravitational-wave observations, one can constrain on the

neutron-star matter EOS. Once the neutron-star EOS is known, one also can measure the relationship between the luminosity distance and the redshift of the binary using only the information of the gravitational waveform through the tidal deformation of the inspiraling neutron stars [19] with more refined detectors such as Einstein telescope [20]. Therefore, modeling the gravitational waveform in NS-NS inspirals including tidal effects is important not only from astrophysical point of view but also from the viewpoint of nuclear physics and cosmology.

For the early stage of NS-NS inspirals ($f \lesssim 400 \text{ Hz}$), a post Newtonian (PN) gravitational waveform was derived by Flanagan and Hinderer including the leading-order tidal effects [21]. It shows that the tidal interaction affects the evolution of the gravitational-wave phase only through a single parameter, namely the tidal deformability of a neutron star, up to the leading order. They also showed that the tidal deformability of a neutron star could be measurable by the advanced gravitational-wave detectors by using the gravitational-wave signals for 10 – 400 Hz, if the tidal deformability of a neutron star is sufficiently large or if we observe an event with a high signal-to-noise ratio (see also Ref. [22]).

More recently, focusing on the late stage of NS-NS inspirals ($f > 400 \text{ Hz}$), Damour and his collaborators [23] explored the measurability of the tidal deformability with the advanced gravitational-wave detectors. They used an effective one body (EOB) formalism for modeling the waveform in NS-NS inspirals including tidal effects up to 2PN order. They concluded that the tidal deformability of a neutron star can be measured by the advanced gravitational-wave detectors for the gravitational-wave signals of which the signal-to-noise ratio is higher than 16 for any EOS that satisfies the constraint of the maximum mass $\geq 1.97M_{\odot}$ [24]. The key assumption of their study is that the EOB formalism is valid up to the contact point of the two neutron stars.

In the stage just before the merger, nonlinear hydro-

dynamics effects play a crucial role for the evolution of NS-NS binaries [25]. In addition, higher-PN tidal corrections may yield a pole-like behavior of the tidal interactions near the last unstable orbit [26].

For better understanding the precise motion and the waveform in this late inspiral stage, a numerical-relativity (NR) simulation is probably the best approach (see, e.g., Refs. [27–29] for a review of this field). Recently, long-term simulations for NS-NS inspirals were performed by three groups [30–32] aiming at the derivation of accurate gravitational waveforms for the late inspiral stage. Baiotti and his collaborators performed a NR simulation employing a Γ -law EOS and compared the resulting waveforms of the *highest* resolution simulation with the analytic models calculated in the EOB and Taylor T4 formalisms [30, 33]. They suggested that the tidal effects might be significantly amplified by higher-PN tidal corrections even in the early inspiral phase.

Bernuzzi and his collaborators performed a simulation with Γ -law EOS ($\Gamma = 2$, and the compactness of a neutron star is 0.14) [34, 35]. In Ref. [34], they studied the convergence of the numerical results for NS-NS inspirals. They concluded that the convergence of the simulation is second order up to contact. They also compared the resulting *extrapolated* waveform with that of the Taylor T4 formalism for the point-particle approximation and for including the tidal corrections. They found that the accumulated phase difference is about 1.5 radian at contact for a particular model of the NS-NS binary. In the subsequent paper [35], they compared the waveform derived by the *highest* resolution simulation with the waveform calculated in the EOB formalism. They found that the EOB formalism including tidal corrections up to the next-to-next-to leading order is currently the most robust way to describe the waveform of NS-NS inspirals. In addition, they excluded the huge amplification of the tidal corrections suggested in Ref. [30].

In this paper, we study NS-NS inspirals by NR simulations with three different EOSs and compare the *extrapolated* NR waveforms with those calculated in the EOB and Taylor T4 formalisms. Here we extrapolate NR data with a new extrapolation procedure, the time and phase extrapolation. For studying the dependence of the tidal effects on the neutron-star matter EOS, we employ a piecewise-polytropic EOS of Ref. [36], which can approximately describe the EOS based on nuclear theoretical calculations and more realistic than Γ -law EOS adopted in Refs.[30, 34, 35]. In this paper, (i) we obtain the physical gravitational-wave phase by extrapolation; (ii) we then compare the *extrapolated* waveforms with those of the analytic models calculated in the Taylor T4 and EOB formalisms; (iii) we clarify the tidal effects on the gravitational-wave phase and show the validity of the analytic modeling in the late inspiral phase.

The paper is organized as follows. In Sec. II, we briefly review the analytic modeling of gravitational waves emitted from a tidally interacting binary system. In Sec. III, we summarize the formulation and numerical schemes

employed in our numerical code SACRA, and review the EOS employed in this study. In Sec. IV, we describe our method of data analysis of the numerical waveforms; the radius extrapolation and the resolution extrapolation. In Sec. V, we compare the extrapolated gravitational-wave phase with those derived in the analytic modeling. Section VI is devoted to a summary. Throughout this paper, we adopt the geometrical units of $c = G = 1$ where c and G are the speed of light the gravitational constant respectively.

II. TIDAL EFFECTS IN A BINARY SYSTEM

In this section, we describe analytic models for the calculation of gravitational waves emitted from NS-NS inspirals in close orbits. We briefly summarize the definition of the tidal deformability of a neutron star, and the PN and EOB descriptions of the tidally-interacting dynamics of close NS-NS binaries.

A. Tidal deformability of a neutron star

In a close binary system for which the separation between two stars is a few times larger than the stellar radius, each star is deformed from its hypothetical equilibrium shape in isolation due to the tidal fields. Assuming that neutron stars are spherically symmetric in the zeroth order, such deformation can be described as the linear responses of neutron stars to external tidal fields [37–39], as long as the degree of the tidal deformation is small. In this linear theory, one assumes that the mass quadrupole moment of a star, Q_{ij} , is proportional to the external quadrupolar tidal fields \mathcal{E}_{ij} as,

$$Q_{ij} = -\lambda \mathcal{E}_{ij}, \quad (1)$$

where λ is the quadrupolar tidal deformability of the star. This relation is called the *adiabatic* approximation for the tidal deformation of a star, which is valid only when the time scale in the change of the weak tidal field is much longer than the dynamical time scale of the star. The tidal deformability is related to the quadrupolar tidal Love number k_2 by

$$\lambda = \frac{2}{3} R^5 k_2, \quad (2)$$

where R is the radius of the (spherical) star in isolation. For a given EOS and a central density, one can calculate the quantities mass, R , k_2 , and λ of neutron stars by solving the Tolman-Oppenheimer-Volkoff equations and the metric perturbation equations [37, 38].

B. The post-Newtonian description for the motion of a tidally interacting binary

The motion of tidally interacting NS-NS binaries in close orbits is affected by the stellar internal structure.

As long as the degree of the tidal interaction is small, the correction of this effect can be described only through the tidal deformability λ [40]. The evolution of the orbital angular velocity in the inspiral of a tidally interacting binary is described by

$$\frac{dx}{dt} = F(x, M_A, M_B, \lambda_A, \lambda_B), \quad (3)$$

where $x = (M\omega)^{2/3}$ with ω being the angular velocity of the binary and M being the total ADM mass at the infinite separation. The subscript (A or B) refers to each component of the binary. The function F can be decomposed into the following two parts,

$$F = F_{\text{pp}}(x, M_A, M_B) + F_{\text{tidal}}(x, M_A, M_B, \lambda_A, \lambda_B), \quad (4)$$

where F_{pp} is the contribution of the point-particle part, and F_{tidal} is the contribution associated with the tidal interactions. In this work, we adopt the Taylor T4 approximant for the F_{pp} [41],

$$\begin{aligned} F_{\text{pp}}^{\text{T4}} = & \frac{64\nu}{5M} x^5 \left[1 - \left(\frac{743}{336} + \frac{11}{4}\nu \right) x + 4\pi x^{3/2} \right. \\ & + \left(\frac{34103}{18144} + \frac{13661}{2061}\nu + \frac{59}{18}\nu^2 \right) x^2 - \left(\frac{4159}{672} + \frac{189}{8}\nu \right) \pi x^{5/2} \\ & + \left\{ \frac{16447322263}{139708800} - \frac{1712}{105}\gamma - \frac{56198689}{217728}\nu \right. \\ & + \frac{541}{896}\nu^2 - \frac{5605}{2592}\nu^3 + \frac{\pi^2}{48} (256 + 451\nu) - \frac{856}{105} \ln(16x) \left. \right\} x^3 \\ & + \left. \left(-\frac{4415}{4032} + \frac{358675}{6048}\nu + \frac{91495}{1512}\nu^2 \right) \pi x^{7/2} \right], \end{aligned} \quad (5)$$

where $\nu = M_A M_B / M^2$ is the symmetric mass ratio, and $\gamma = 0.577126\dots$ is an Euler's constant. As shown by Boyle and his collaborators [41], the evolution of the angular velocity of the Taylor T4 approximant agrees well with those of the NR simulations for the inspiral of equal-mass non-spinning binary black holes up to $M\omega \sim 0.1$. We adopt the tidal part which is derived by Vines and his collaborators [40] as follows,

$$\begin{aligned} F_{\text{tidal}} = & \frac{32M_A \lambda_B}{5M^7} \left[12 \left(1 + 11 \frac{M_A}{M} \right) x^{10} \right. \\ & + \left(\frac{4421}{28} - \frac{12263}{28} \frac{M_B}{M} + \frac{1893}{2} \left(\frac{M_B}{M} \right)^2 \right. \\ & \left. \left. - 661 \left(\frac{M_B}{M} \right)^3 \right) x^{11} \right] + (A \leftrightarrow B). \end{aligned} \quad (6)$$

In particular, for the case of equal-mass binaries, F_{tidal} is given by

$$F_{\text{tidal}} = \frac{52}{5M} x^{10} k_2 C^{-5} \left(1 + \frac{5203}{4368} x \right), \quad (7)$$

where $C = M_A / R_A (= M_B / R_B)$ is the compactness of the neutron star. Although the tidal interaction affects

NS-NS inspirals only at 5PN order, its coefficient is of order 10^4 for typical neutron stars of radius 10 – 15 km, $k_2 \sim 0.1$, and $C \sim 0.14 - 0.20$, and thus, it plays an important role in the late inspiral stage.

C. Effective one body formalism for the motion of a tidally interacting binary

The EOB formalism maps the dynamics of two point particles to the Hamiltonian dynamics of an effective particle moving in an effective external potential [43–45]. Because the EOB formalism goes beyond the adiabatic approximation for binary inspirals, it is suitable for describing the late inspiral stage of a binary, for which the adiabatic approximation is not very accurate. In this work, we employ the resummed EOB description which is largely the same as that in Ref. [46] for the point-particle part and as that in Ref. [23] for the tidal part.

The EOB effective metric is defined by

$$ds_{\text{eff}}^2 = -A(r)dt^2 + \frac{D(r)}{A(r)}dr^2 + r^2 (d\theta^2 + \sin^2\theta d\phi^2), \quad (8)$$

where (t, r, ϕ) are the dimensionless coordinates and their canonical momenta are (p_r, p_ϕ) . We replace the radial canonical momentum p_r with the canonical momentum p_{r_*} , where the tortoise-like radial coordinate r_* is defined by

$$\frac{dr_*}{dr} = \frac{\sqrt{D(r)}}{A(r)}. \quad (9)$$

Then the binary dynamics can be described by the EOB Hamiltonian

$$\hat{H}_{\text{real}}(r, p_{r_*}, p_\phi) = \frac{1}{\nu} \sqrt{1 + 2\nu (\hat{H}_{\text{eff}} - 1)} - \frac{1}{\nu}, \quad (10)$$

where the effective Hamiltonian is defined by,

$$\hat{H}_{\text{eff}} = \sqrt{p_{r_*}^2 + A(r) \left(1 + \frac{p_\phi^2}{r^2} + 2(4 - 3\nu)\nu \frac{p_{r_*}^4}{r^2} \right)}. \quad (11)$$

The metric component $A(r)$ is decomposed into two parts as

$$A(r) = A_{\text{pp}}(r) + A_{\text{tidal}}(r), \quad (12)$$

where $A_{\text{pp}}(r)$ is the point-particle part and $A_{\text{tidal}}(r)$ is associated with the tidal effects. The point-particle part up to the 5PN order is given by

$$\begin{aligned} A_{\text{pp}}(r) = P_5^1 \left[1 - 2u + 2\nu u^3 + a_4 \nu u^4 \right. \\ \left. + a_5 \nu u^5 + a_6 \nu u^6 \right], \end{aligned} \quad (13)$$

where $a_4 = 94/3 - 41\pi^2/32$, $u = 1/r$, and P_5^1 denotes a (1, 5) Pade approximant. In the definition of $A(r)$, there

are two analytically undetermined parameters (a_5, a_6), which correspond to the 4PN and 5PN corrections. Here, we adopt the values $(a_5, a_6) = ((-5.828 - 143.5\nu + 477\nu^2)\nu, 184\nu)$ following Ref. [46].

The tidal part of $A(r)$ is given by

$$A_{\text{tidal}}(r) = \sum_{l \geq 2} -\kappa_l u^{2l+2} \hat{A}_l(u), \quad (14)$$

where \hat{A}_l includes the PN tidal contributions for each multipole, and κ_l is its coefficient. This coefficient is related to the tidal Love number k_l and the compactness of two stars by

$$\kappa_l = 2 \frac{M_B M_A^{2l}}{M^{2l+1}} \frac{k_l^A}{C_A^{2l+1}} + (A \leftrightarrow B). \quad (15)$$

In this work, we include only the tidal-interaction part of the lowest multipole $l = 2$. Up to the next-to-leading order, $\hat{A}_{l=2}$ is given by [42]

$$\hat{A}_{l=2}^{(A)}(u) = 1 + \alpha_1^{(A)} u, \quad (16)$$

where $\alpha_1^{(A)} = 5M_A/2M$. The tidal-interaction term up to the 2PN corrections is currently known, and the coefficient α_2 is larger than α_1 [26]. In addition, an analysis in the test-mass limit ($M_A \ll M_B$) suggests that the tidal part $\hat{A}_{l=2}^{(A)}$ has the pole-like behavior near the last unstable orbit located at $3M_B$ (the light ring orbit). Thus, it is reasonable to expect that the higher-PN corrections would amplify the tidal effects. In this work, we employ the resummed version of the tidal metric including up to the next-to-next-to-leading order given by [26]

$$\hat{A}_{l=2}^{(A)}(u) = 1 + \alpha_1^{(A)} u + \alpha_2^{(A)} \frac{u^2}{1 - \hat{r}_{\text{LR}} u}, \quad (17)$$

where

$$\alpha_2^{(A)} = 337M_A^2/28M^2 + M_A/8M + 3, \quad (18)$$

and

$$\hat{r}_{\text{LR}}(\nu, \kappa_2) = 3 \left[1 - \frac{5\nu}{3^3} + \frac{4}{3^6} \kappa_2 + O(\nu^2, \kappa_2\nu, \kappa_2^2) \right], \quad (19)$$

is the dimensionless radius of the light ring orbit.

For the calculation of the binary orbit, we solve the EOB Hamilton equations [43–45]

$$\frac{dr}{dt} = \frac{A(r)}{\sqrt{D_3^0(r)}} \frac{\partial \hat{H}_{\text{real}}}{\partial p_{r_*}}, \quad (20)$$

$$\frac{d\phi}{dt} = \frac{\partial \hat{H}_{\text{real}}}{\partial p_\phi}, \quad (21)$$

$$\frac{dp_{r_*}}{dt} = -\frac{A(r)}{\sqrt{D_3^0(r)}} \frac{\partial \hat{H}_{\text{real}}}{\partial r} + \hat{\mathcal{F}}_\phi \frac{p_{r_*}}{p_\phi}, \quad (22)$$

$$\frac{dp_\phi}{dt} = \hat{\mathcal{F}}_\phi, \quad (23)$$

where $D_3^0(r)$ is a (0, 3) Pade approximant of $D(r)$ [46], and $\hat{\mathcal{F}}_\phi$ is the radiation-reaction force given by

$$\hat{\mathcal{F}}_\phi = -\frac{1}{8\pi\nu\hat{\omega}} \sum_{l=2}^8 \sum_{m=1}^l (m\hat{\omega})^2 \left| \frac{R}{M} h_{lm} \right|^2. \quad (24)$$

Here, $\hat{\omega} = d\phi/dt$, h_{lm} denote the multipolar waveforms, and R is the radius of extracting gravitational waves. The waveforms are described by

$$h_{lm} = h_{lm}^0 + h_{lm}^{\text{tidal,A}} + h_{lm}^{\text{tidal,B}}, \quad (25)$$

where h_{lm}^0 denotes the inspiral and plunge waveform for a binary black hole of mass M_A and M_B , and $h_{lm}^{\text{tidal,A}}$ is the contribution due to the tidal deformation of star A. In this work, h_{lm}^0 is given by Eqs. (13)–(22) of Ref. [46] and $h_{lm}^{\text{tidal,A}}$ is basically given by Eqs. (A14)–(A17) of Ref. [23]. Because the 2PN term associated with the tidal effect in the waveform is currently unknown, we include the contributions of the tidal effect to $h_{lm}^{\text{tidal,A}}$ up to the 1PN term even for the case that the next-to-next-to-leading order term is taken into account in the radial potential.

III. NUMERICAL RELATIVITY SIMULATION

In this section, we briefly describe the formulation and the numerical schemes of our NR simulation employed in this work.

A. Evolution and Initial Condition

We follow the inspiral and merger of NS-NS binaries using our NR code, called SACRA, for which the details are described in Ref. [47]. SACRA employs a moving puncture version of the Baumgarte-Shapiro-Shibata-Nakamura formalism [48–50] to solve Einstein's equations imposing the equatorial symmetry (and π -symmetry for the equal-mass cases). In the numerical simulations, a fourth-order finite differencing scheme in space and time is used implementing an adaptive mesh refinement algorithm. At refinement boundaries, a second-order interpolation scheme is partly adopted. The advection terms are evaluated by a fourth-order non-centered finite differencing [51]. A fourth-order Runge-Kutta method is employed for the time evolution. For the hydrodynamics, we employ a high-resolution central scheme based on Kurganov and Tadmor scheme [52] with a third-order piecewise parabolic interpolation and with a steep minmod limiter.

In this work, we prepare seven refinement levels both for efficiently resolving two neutron stars by the finest-resolution domains and for extracting gravitational waves in a local wave zone. More precisely, two sets of four finer domains comoving with each neutron star cover

TABLE I: Key parameters for the initial models adopted in the present numerical simulation. M_0 is the sum of the ADM masses of two neutron stars in isolation; ν is the symmetric mass ratio; M_0^{ADM} and J_0^{ADM} are the ADM mass and angular momentum of the system, respectively; M_* is the baryon rest mass; ω_0 is the angular velocity. We also show the setup of the grid structure of our AMR algorithm. $\Delta x = h_6 = L/(2^6 N)$ ($N = 60$) is the grid spacing for the highest-resolution domain with L being the location of the outer boundaries for each axis. N specifies the grid size of the simulation with maximum $N = 60$. κ_2 is the parameter related to the tidal deformability. ω_{contact} is the orbital angular velocity at contact of the two neutron stars (see Sec. V. B). Here we use the unit $M_\odot = 1$

Model	M_0	ν	M_0^{ADM}	J_0^{ADM}	M_*	$M\omega_0$	$\Delta x/M$	κ_2	$M\omega_{\text{contact}}$	N
APR4	2.7	0.25	2.68	7.65	3.00	0.019	0.0438	62.3	0.151	(42,48,54,60)
H4	2.7	0.25	2.68	7.66	2.94	0.019	0.0560	215	0.112	(42,48,54,60)
MS1	2.7	0.25	2.68	7.67	2.92	0.019	0.0595	332	0.103	(42,48,54,60)
APR4-1215	2.7	0.24691358	2.68	7.28	3.01	0.0221	0.0438	65.8	0.151	(40,50,60)
H4-1215	2.7	0.24691358	2.68	7.56	2.94	0.019	0.0560	207	0.114	(40,50,60)

TABLE II: Parameters of the piecewise-polytropic EOS, the compactness, and the tidal Love number of the neutron star of mass $1.35M_\odot$.

EOS	$\log P_1(\text{dyne/cm}^2)$	Γ_1	Γ_2	Γ_3	$C(1.35)$	$k_2(1.35)$
APR4	34.269	2.830	3.445	3.348	0.179	0.091
H4	34.669	2.909	2.246	2.144	0.146	0.115
MS1	34.858	3.224	3.033	1.325	0.138	0.133

the region of their vicinity. The other three coarser domains cover both neutron stars by a wider domain with their origins fixed approximately at the center of the mass of the binary. Each refinement domain consists of the uniform, vertex-centered Cartesian grids with $(2N + 1, 2N + 1, N + 1)$ grid points for (x, y, z) with the equatorial plane symmetry at $z = 0$ imposed. The half of the edge length of the largest domain (i.e., the distance from the origin to outer boundaries along each axis) is denoted by L which is chosen to be larger than λ_0 , where $\lambda_0 = \pi/\omega_0$ is the initial wave-length of gravitational waves and ω_0 is the initial orbital angular velocity. The grid spacing for each domain is $h_l = L/(2^l N)$, where $l = 0 - 6$. In this work, we choose $N = 60, 54, 48$, and 42 for the resolution study. With the highest grid resolution, the semimajor diameter of each neutron star is covered by about 100 grid points.

We prepare NS-NS binaries in quasiequilibrium states for the initial condition of numerical simulations by using a spectral-method library, LORENE [53]. To track more than 8 orbits, the orbital angular velocity of the initial configuration is chosen to be $M\omega_0 = 0.019$ ($f = 400\text{Hz}$ for $M = 2.7M_\odot$), where M_\odot is the solar mass. The neutron stars are assumed to have an irrotational velocity field, which is believed to be an astrophysically realistic configuration [54, 55]. The parameters for the initial models are listed in Table I.

B. Equation of State

In this work, we employ a parameterized piecewise-polytropic EOS proposed by Read and her collaborators [36]. This EOS is written in terms of four segments of polytropes

$$P = K_i \rho^{\Gamma_i} \quad (26)$$

(for $\rho_i \leq \rho < \rho_{i+1}$, $0 \leq i \leq 3$),

where ρ is the rest-mass density, P is the pressure, K_i is a polytropic constant, and Γ_i is an adiabatic index. At each boundary of the piecewise polytropes, $\rho = \rho_i$, the pressure is required to be continuous, i.e., $K_i \rho_i^{\Gamma_i} = K_{i+1} \rho_i^{\Gamma_{i+1}}$. Read and her collaborators determine these parameters in the following manner [36]. First, they fix the EOS of the crust as $\Gamma_0 = 1.357$ and $K_0 = 3.594 \times 10^{13}$ in cgs units. Then they determine $\rho_2 = 1.85\rho_{\text{nucl}}$ and $\rho_3 = 3.70\rho_{\text{nucl}}$ where $\rho_{\text{nucl}} = 2.7 \times 10^{14} \text{g/cm}^3$ is the nuclear saturation density. With this preparation, they choose the following four parameters as a set of free parameters: $\{P_1, \Gamma_1, \Gamma_2, \Gamma_3\}$. Here P_1 is the pressure at $\rho = \rho_2$, and from this, K_1 and K_i are determined by $K_1 = P_1/\rho_2^{\Gamma_1}$ and $K_{i+1} = K_i \rho_i^{\Gamma_i - \Gamma_{i+1}}$. Therefore the EOS is specified by choosing the four parameters $\{P_1, \Gamma_1, \Gamma_2, \Gamma_3\}$. In this work, we choose the three sets of piecewise-polytropic EOS as listed in Table II.

We describe the low-density part of the EOS only with a single polytrope, because the elastic property of the crust yields a very small correction to the tidal number [58]. Thus, our approximate treatment for the low-density part is acceptable.

C. Extraction of Gravitational waves

Gravitational waves are extracted by calculating the complex Weyl scalar Ψ_4 [47] from which gravitational waveforms are determined by

$$h_+(t) - ih_\times(t) = - \lim_{r \rightarrow \infty} \int^t dt' \int^{t'} dt'' \Psi_4(t'', r). \quad (27)$$

Here we omit arguments θ and ϕ . In the spherical coordinate (r, θ, ϕ) , Ψ_4 can be expanded in the form

$$\Psi_4(t, r, \theta, \phi) = \sum_{lm} \Psi_4^{lm}(t, r) {}_{-2}Y_{lm}(\theta, \phi), \quad (28)$$

where ${}_{-2}Y_{lm}$ are spin-weighted spherical harmonics of weight -2 and Ψ_4^{lm} are expansion coefficients defined by this equation. In this work, we focus only on the $(l, |m|) = (2, 2)$ mode. The gravitational-wave phase ϕ_{NR} is defined by

$$\Psi_4^{22}(t, r) = A_{22}(t, r) e^{i\phi_{\text{NR}}(t, r)}, \quad (29)$$

where A_{22} denotes the amplitude and it is real. We evaluate Ψ_4 at a finite spherical-coordinate radius $r/M_\odot = 200, 240, 300, \text{ and } 400$. To compare the waveforms extracted at different radii, we use the retarded time defined by

$$t_{\text{ret}} = t - r_*. \quad (30)$$

Here, r_* is the tortoise coordinate defined by

$$r_* = r_A + 2M \ln \left(\frac{r_A}{2M} - 1 \right), \quad (31)$$

where $r_A = \sqrt{A/4\pi}$ with A being the proper surface area of the extraction sphere.

IV. DATA ANALYSIS OF NUMERICAL-RELATIVITY SIMULATIONS

The extrapolation with respect to the extraction radius and grid resolution plays a key role to obtain the physical waveforms in NS-NS inspirals from the results of NR simulations. Here, we focus in particular on deriving the accurate gravitational-wave phase by extrapolation because it carries the most important information in the matched filtering for data analysis. Thus, the goal of this section is to construct the extrapolated gravitational-wave phase.

A. Extrapolation to infinity

Because gravitational waves are extracted at finite radii, the extracted waveform does not fully agree with the waveform at infinity. For obtaining the hypothetical gravitational-wave phase at infinity, we first need to estimate the error due to the finite-radii extraction and then

to extrapolate the gravitational-wave phase to infinity. For this purpose, we assume that the gravitational-wave phase is described by a polynomial [41],

$$\phi(t_{\text{ret}}, r) = \phi^{(0)}(t_{\text{ret}}) + \sum_{i=1}^s \frac{\phi^{(i)}(t_{\text{ret}})}{r^i}. \quad (32)$$

Here, $\phi^{(0)}(t_{\text{ret}})$ is considered to be the gravitational-wave phase extrapolated at $r \rightarrow \infty$, and $(s+1)$ is the number of extraction radii used. We determine it by extrapolating the gravitational-wave phases extracted at $r/M_\odot = 200, 240, 300, \text{ and } 400$.

Figure 1 shows the differences among the hypothetically extrapolated gravitational-wave phases at infinity obtained by different numbers of extrapolation radius, s . The curves labeled by $1-3 (= s-1)$ in Fig. 1 denote the differences between a radius-extrapolated gravitational-wave phase with the $(s-1)$ -th order polynomial and that with the s -th order one. Here, we set the phase difference to be zero at the merger. Note that the difference between the $(s-1)$ -th and s -th order extrapolated gravitational-wave phases accumulates mainly just after the contact of the two stars and its value is less than about 0.5 radian. In this paper, we do not pay attention to the gravitational-wave phase after contact of the two stars. As shown in the next subsection, furthermore, this accumulated gravitational-wave phase difference of the radius extrapolation is much smaller than the magnitude of other error sources. Therefore, in this paper, we neglect the phase error associated with the finite-radius extraction, and use the resolution-extrapolated gravitational-wave phase with the extracted radius $r/M_\odot = 400$ as the extrapolated wave phase. We note however that in a high-resolution study, the error associated with the finite-radius extraction could be comparable to or smaller than the error due to the finite grid resolution.

B. Extrapolation to infinite resolution

A NR waveform is derived as a solution of discretized Einstein's equations and hydrodynamics equations. Associated with the finite differencing, a truncation error is yielded. For the purpose of comparing the NR waveform with the PN and EOB waveforms, we have to obtain a hypothetically physical waveform by extrapolating the NR waveform obtained in the finite grid resolution for the limit of the infinite grid resolution. The order of the convergence of our NR simulation with respect to the grid spacing is found to be about 1.8. Because the order of the convergence has an uncertainty, we conservatively assume that the order of the convergence is 1.8 ± 0.2 in the following.

For understanding the convergence property of the numerical results, we check the convergence for the evolution of the gravitational-wave frequency performing simulations with four different grid resolutions (see Fig. 2

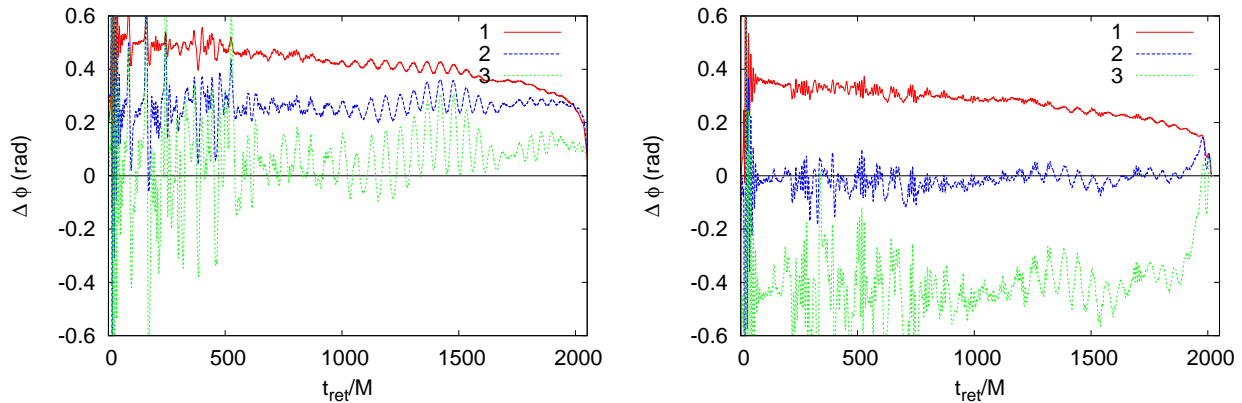


FIG. 1: The phase errors for APR4 (left) and H4 (right). The curve 1 denotes the difference between the gravitational-wave phase extracted at $r/M_\odot = 400$ and an extrapolated gravitational-wave phase obtained using the data at $r/M_\odot = 300$ and 400. The curve 2 denotes the difference between the extrapolated gravitational-wave phase obtained using the data at $r/M_\odot = 300$ and 400 and that obtained using the data at $r/M_\odot = 240, 300,$ and 400. The curve 3 denotes the difference between the extrapolated gravitational-wave phase obtained using the data at $r/M_\odot = 240, 300,$ and 400 and that obtained using the data at $r/M_\odot = 200, 240, 300,$ and 400.

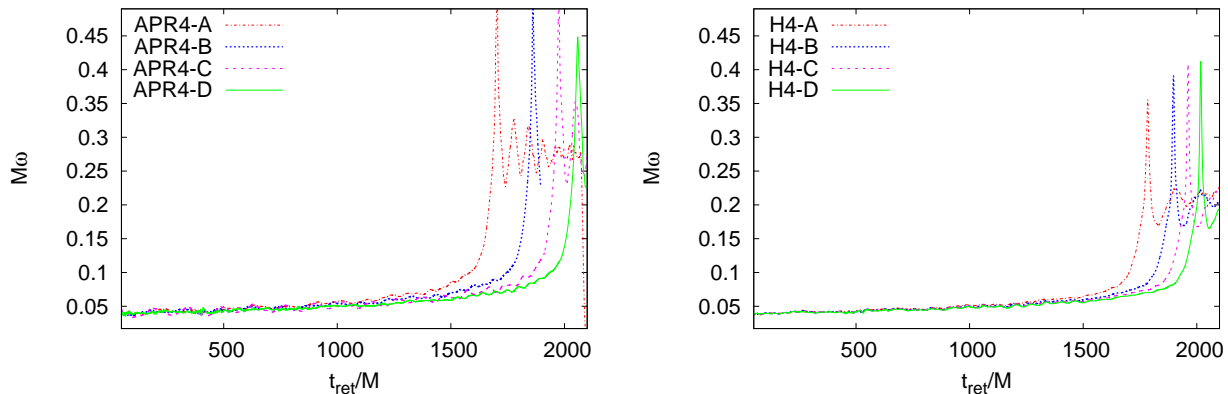


FIG. 2: The evolution of gravitational-wave angular velocity for four different resolutions for APR4 (left panel) and H4 (right panel). The curves with marks A, B, C, and D denote the results for the simulations with $N = (42, 48, 54, 60)$, respectively.

for gravitational-wave angular velocity). Here, we refer to the data for $N = (42, 48, 54, 60)$ as (A, B, C, D). Although the gravitational-wave frequencies agree with each other at $t_{\text{ret}} = 0$, their subsequent evolution disagrees with each other. Obviously, the gravitational-wave frequency in the lower grid resolution evolves more rapidly than that in the higher grid resolution. The rapid evolution for the lower-resolution simulations may be ascribed to larger numerical dissipation of the angular momentum.

However, one can find the similarity among four curves of the gravitational-wave frequency for the different grid resolutions and this enables us to obtain an extrapolated waveform. To show this similarity, we normalize the time variable by using the time at the onset of the merger,

which is defined by $t_m(\Delta x) = t|_{\omega_{\text{max}}}(\Delta x)$:

$$t \rightarrow \tilde{t}(t) = \frac{t}{\Lambda(\Delta x)}. \quad (33)$$

Here, $\Lambda(\Delta x) = t_m(0)/t_m(\Delta x)$, Δx is the grid spacing of the simulation ($\propto N^{-1}$), and $t_m(0)$ is the extrapolated merger time. For obtaining the extrapolated merger time, we assume that the merger time as a function of grid resolutions is described by a binomial

$$t_m(\Delta x) = t_m(0) + K(\Delta x)^n, \quad (34)$$

where $t_m(0)$, n , and K are constants which are determined by the least-square fitting method. We find that the best fitted value of n is ≈ 1.8 with a dispersion ~ 0.2 , and thus, we set the order of the convergence n is to be 1.8 ± 0.2 . The resulting fitted values for

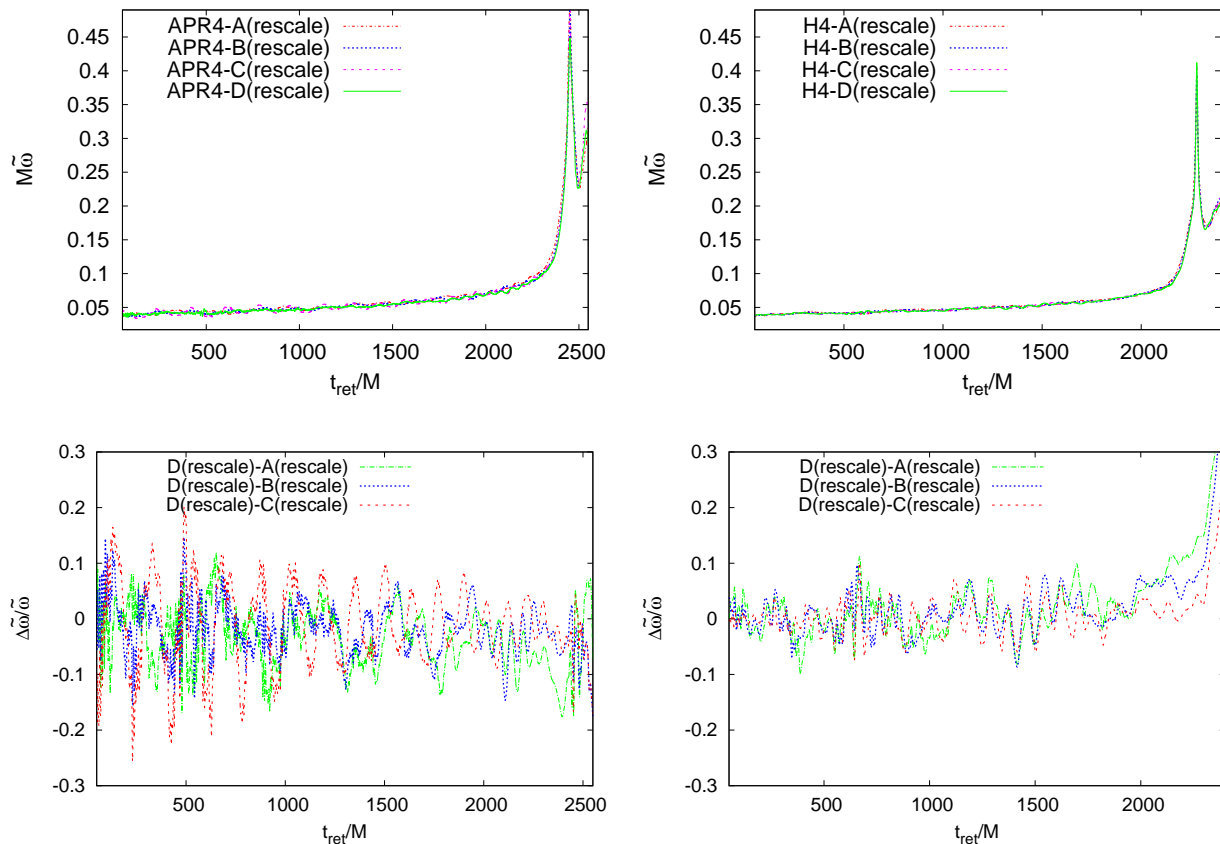


FIG. 3: Convergence of the rescaled gravitational-wave angular velocity. *Upper panels:* the evolution curves of the rescaled gravitational-wave angular velocity for APR4 (left panel) and H4 (right panel). *Lower panels:* the difference in the rescaled gravitational-wave frequency between different resolutions for APR4 (left panel) and H4 (right panel). Here we choose $n = 1.8$.

$n = (1.6, 1.8, 2.0)$ are $t_m(0) = (2521M, 2452M, 2397M)$ for APR4, $t_m(0) = (2391M, 2274M, 2238M)$ for H4, and $t_m = (2145M, 2145M, 2091M)$ for MS1.

We define the rescaled gravitational-wave frequency by

$$\tilde{\omega}(t, \Delta x) \equiv \omega(\tilde{t}(t), \Delta x). \quad (35)$$

The evolution curves of the rescaled gravitational-wave frequency $\tilde{\omega}$ for the different grid resolutions agree with each other, as shown in the upper two panels of Fig. 3 (here, we set $n = 1.8$). The differences among the rescaled gravitational-wave frequencies of the different grid resolutions are within $\sim 10\%$ for APR4 and $\sim 5\%$ for H4, as shown in the lower panels of Fig. 3. Therefore, we conclude that the numerical results for the gravitational-wave frequency (angular velocity) is written in the form

$$\tilde{\omega}(t, \Delta x) = \tilde{\omega}(t, 0) + \omega_r(t, \Delta x), \quad (36)$$

where $\omega_r(t, \Delta x)$ is a function that depends on the grid resolution, which should have been eliminated systematically by extrapolation. However, because the value of $\omega_r(t, \Delta x)$ randomly fluctuates, it cannot be eliminated by

extrapolation at each given moment. Thus, the extrapolated gravitational-wave frequency can be only approximately obtained by simply rescaling the time variable of the simulations.

We proceed to extrapolate the rescaled gravitational-wave phase, which will be compared with the gravitational-wave phases derived in the PN and EOB approaches in the next section. We define the rescaled gravitational-wave phase as

$$\tilde{\phi}(t, \Delta x) \equiv \int_0^t \tilde{\omega}(t', \Delta x) dt'. \quad (37)$$

Substituting Eq. (35) into this equation yields

$$\tilde{\phi}(t, \Delta x) = \Lambda(\Delta x)\phi(\tilde{t}, \Delta x), \quad (38)$$

and combining Eq. (36) and Eq. (37) yields

$$\tilde{\phi}(t, \Delta x) = \tilde{\phi}(t, 0) + \int_0^t \epsilon(t', \Delta x) dt', \quad (39)$$

where $\tilde{\phi}(t, 0)$ is the extrapolated gravitational-wave phase. Assuming the second term in the right-hand side

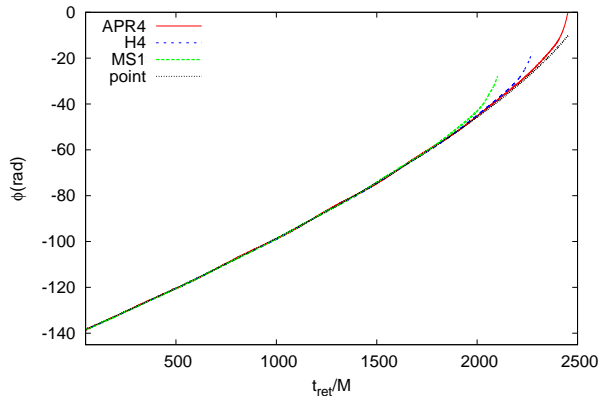


FIG. 4: The extrapolated gravitational-wave phase for the three EOSs. Here, we set the order of the convergence to be 1.8.

of this equation can be described as $\phi_r(t)\Delta x^n$, we obtain

$$\Lambda(\Delta x)\tilde{\phi}(\tilde{t}, \Delta x) = \tilde{\phi}(t, 0) + \phi_r(t)\Delta x^n. \quad (40)$$

Here $\tilde{\phi}(t, 0)$ and $\phi_r(t)$ are functions which are determined by the least-square fitting of the numerical data $\phi_{\text{NR}}(\tilde{t}, \Delta x)$. We again set the order of the convergence n to be 1.8 ± 0.2 . Figure 4 shows the evolution curves of the extrapolated gravitational-wave phase for the different EOS.

The differences in the rescaled gravitational-wave phase $\tilde{\phi}_{\text{NR}}(t, \Delta x)$ obtained for runs with the different grid resolutions and the extrapolated gravitational-wave phase $\tilde{\phi}(t, 0)$ for $n = 1.8$ are shown in Fig. 5. The accumulated difference between the extrapolated gravitational-wave phase and that of the highest grid resolution at the onset of the merger is ~ 8 radian for APR4 and ~ 3 radian for H4. These values imply that the simulation for the neutron star which has the larger radius is relatively well convergent. These phase differences are much larger than the possible error in the gravitational-wave phase associated with the finite-radius extraction, $\lesssim 0.5$ radian. Thus, we conclude that the resolution extrapolation of the gravitational-wave phase is essential to construct the extrapolated physical waveform for our current NR simulations. The lower panels in Fig. 5 show the difference between the gravitational-wave phase of the resolution D, $\tilde{\phi}_{\text{NR}}(t, \Delta x_D)$, and the one which is obtained by extrapolating the gravitational-wave phase of the resolutions A, B, and C to the resolution D, $\tilde{\phi}(t, \Delta x_D)$. The difference $\Delta\phi$ is within 0.15 radian up to the merger. Here, this error is caused mainly by a modulation associated with an unphysical orbital eccentricity. The upper panels of Fig. 6 show the evolution curves of the extrapolated gravitational-wave phase for the different choice of n .

For the brief check of the validity of the extrapolation,

we calculate the dispersion $\sigma(t)$ of the extrapolation as

$$\sigma(t)^2 = \frac{1}{N_{\text{R}}} \sum_{i=1}^{N_{\text{R}}} \left(\tilde{\phi}(t, \Delta x_i) - \tilde{\phi}_{\text{NR}}(t, \Delta x_i) \right)^2, \quad (41)$$

where $\tilde{\phi}_{\text{NR}}(\tilde{t}, \Delta x_i)$ is the rescaled gravitational-wave phase of the numerical data, $i = 1 \sim N_{\text{R}}$ denote the numerical run with the different grid resolutions, e.g. $N = (42, 48, 54, 60)$, and N_{R} is the total number of them, e.g. $N_{\text{R}} = 4$. As shown later, the value of the dispersion is in the range 0.01 radian (in the early part) to 0.4 radian (just before the merger). We regard this dispersion as an error due to the resolution extrapolation. Hereafter we use only the extrapolated quantities and omit the tilde of them.

V. COMPARISON OF THE NR WAVE PHASE WITH THE PN AND EOB WAVE PHASES

A. Matching Procedure

In the analysis, we first match an early part of the gravitational-wave phase obtained by extrapolating NR results, $\phi_{\text{NR}}(t)$, with that of the analytic ones, $\phi_{\text{PN}}(t)$ (the wave phase derived in the PN calculation) and $\phi_{\text{EOB}}(t)$ (the wave phase derived in the EOB calculation), by minimizing the following quantity,

$$\begin{aligned} & \int_{t_1}^{t_2} (\Delta\phi(t))^2 dt \\ & = \int_{t_1}^{t_2} (\phi_{\text{NR}}(t) - \phi_{\text{PN/EOB}}(t - t_s) - \phi_s)^2 dt, \end{aligned} \quad (42)$$

where ϕ_s and t_s are the fitting parameters. The initial and final time of the integral, t_1 and t_2 , are chosen as follows. As shown in the previous section, the curve of the extrapolated gravitational-wave phase obtained from the results of NR simulations has a small modulation due to the orbital eccentricity. Thus, (t_1, t_2) are chosen to cover a range between two adjacent local maxima or local minima of the curve in an early part of the gravitational-wave phase. This choice of the matching region allows us to match the gravitational-wave phase numerically obtained with the PN/EOB phases smoothly using the least-square fitting. Here, we choose the two adjacent local minima as the matching boundaries as follows: $(t_1, t_2) = (583M, 1030M)$ for APR4 (which corresponds to $M\omega \in [0.042 : 0.048]$), $(t_1, t_2) = (550M, 1000M)$ for H4 (which corresponds to $M\omega \in [0.042 : 0.046]$), and $(t_1, t_2) = (550M, 960M)$ for MS1.

B. Comparison

We compare ϕ_{NR} with ϕ_{PN} and ϕ_{EOB} which are calculated in several levels of the approximation. The middle

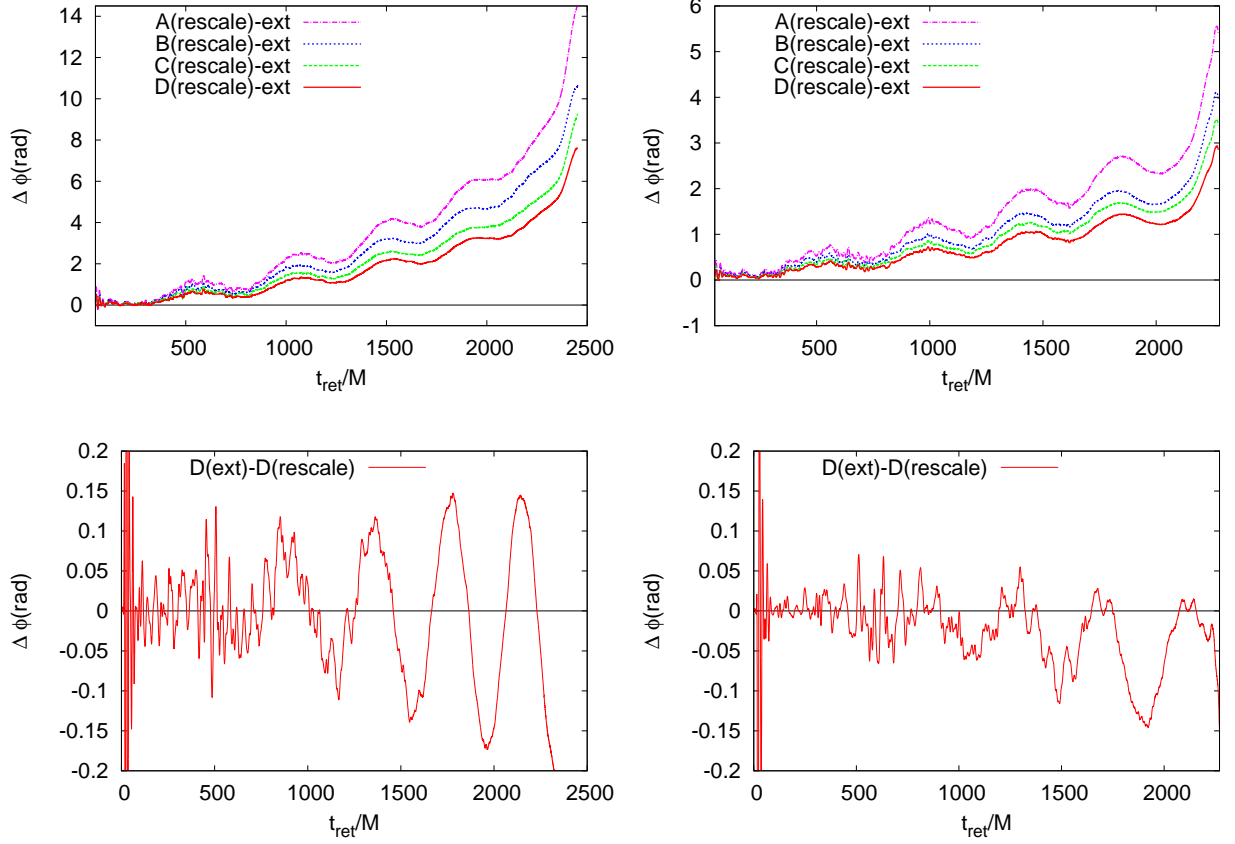


FIG. 5: Convergence of the gravitational-wave phase for APR4 (left) and H4 (right). In the upper panels, the curves show the phase differences between the extrapolated gravitational-wave phase and the rescaled numerical results. Here, we set the order of the convergence n to be 1.8 for deriving the extrapolated gravitational-wave phase. In the lower panels, the curves show the difference between the rescaled gravitational-wave phase in the resolution D and the extrapolated gravitational-wave phase which is obtained by extrapolating the rescaled gravitational-wave phases of the resolution A, B, and C to the resolution D.

panels of Fig. 6 show the difference between ϕ_{NR} and ϕ_{EOB} in which tidal effects up to the next-to-leading order are included. The error bars show the dispersion associated with the least-square fitting in the extrapolation procedure, which is defined by Eq. (41). The three curves show the gravitational-wave phase difference for the three assumed orders of the convergence $n = (1.6, 1.8, 2.0)$. The phase differences are modulated with an amplitude about 0.4 radian due to the unphysical orbital eccentricity. We regard this modulation as a systematic error, which is denoted by the horizontal dashed lines. For comparison, we also plot the gravitational-wave angular velocity evolution in the bottom of Fig. 6. Figure 7–9 shows the difference between ϕ_{NR} and $\phi_{\text{PN/EOB}}$ which are calculated in several levels of the approximation.

In the early stage of the inspiral, i.e., before the time $t_{\text{ret}}/M \lesssim 1500$ ($M\omega \lesssim 0.054$) for APR4, $t_{\text{ret}}/M \lesssim 1300$ ($M\omega \lesssim 0.05$) for H4, and $t_{\text{ret}}/M \lesssim 1200$ ($M\omega \lesssim 0.049$) for MS1, we find that ϕ_{NR} is consistent with ϕ_{PN} and ϕ_{EOB} for any levels of the approximation. In this stage, the point-particle approximation works well and the PN and EOB approaches appear to describe NS-NS

inspirals well even if tidal effects are not taken into account. It is difficult to verify a clear signature of the tidal effects in this early stage due to the modulation of the numerical data and the weakness of the tidal effects.

After the early stage of the inspiral, the binary system proceeds to a tidally-dominated inspiral phase where the tidal interaction becomes strong. In this late inspiral stage, one can see that the difference between ϕ_{NR} and $\phi_{\text{PN/EOB}}$ gradually increases. ϕ_{NR} is larger than $\phi_{\text{PN/EOB}}$ for a given moment, implying binaries in NR simulations evolve faster than those in the PN and EOB calculations.

After the time $t_{\text{ret}}/M \sim 2300$ ($M\omega \sim 0.09$) for APR4, $t_{\text{ret}}/M \sim 2100$ ($M\omega \sim 0.08$) for H4, and $t_{\text{ret}}/M \sim 1950$ ($M\omega \sim 0.075$) for MS1, the difference between ϕ_{NR} and ϕ_{EOB} rapidly increases with increasing time. This corresponds to the transition from the inspiral to the plunge. The orbital angular velocity when two neutron stars come into contact, $M\omega_{\text{contact}}$, is approximately de-

finied by [23]

$$M\omega_{\text{contact}} = 2 \left(\frac{M_A}{M} \frac{1}{C_A} + \frac{M_B}{M} \frac{1}{C_B} \right)^{-3/2}. \quad (43)$$

At the moment of this contact, the accumulated gravitational-wave phase difference between ϕ_{NR} and ϕ_{EOB} including the tidal effects up to the next-to-leading order is ~ 3.3 radian (2.5%) for APR4, ~ 1.9 radian (1.7%) for H4, and ~ 2.1 radian (2.0%) for MS1. If the correction is up to the next-to-next-to-leading order, the phase difference is ~ 2.6 radian (2.0%) for APR4, ~ 1.4 radian (1.3%) for H4, and ~ 1.1 radian (1.1%) for MS1. We find that the EOB approach including the tidal effects up to the next-to-next-to-leading order yields currently the best model for the late stage of NS-NS inspirals. However, the tidal effects are still underestimated for the final inspiral orbit even for the best model of the analytic approaches. Thus, for constructing better waveforms in NS-NS inspirals, this rapid evolution of the gravitational-wave phase should be taken into account.

We compare our results of MS1, of which the compactness is $C = 0.138$, with the results of Ref. [34], for which a neutron-star with $C = 0.14$ is employed. Both results show that the difference between the extrapolated gravitational-wave phase of NR and that of T4 without tidal effects is about 3 radian at contact ($M\omega \sim 0.1$), in the case that the alignment is performed after the first orbit [34]. Therefore our results are consistent with the results of Ref. [34].

Figure 10 and Fig. 11 show the snapshots of the density contour of NS-NS inspirals for APR4 and H4. Here we focus on Fig. 11 as an example. The upper left panel of Fig. 11 plots the density profile of the binary at an early inspiral stage. At this time, the neutron stars have a spherical shape. The ellipticity of the neutron star, which is defined by the ratio of the semi-major axis a_1 to the semi-minor axis a_2 of the star on the equatorial plane, is approximately unity.

The upper right panel of Fig. 11, at $M\omega = 0.056$, plots the configuration of the binary at which the tidal effects seem to be small but cannot be neglected. For this plot, the ellipticity of the star is ~ 1.05 . After this time, the binary system proceeds to the tidally-dominated inspiral phase. In the lower left panel of Fig. 11, two neutron stars are obviously deformed due to the strong tidal fields; the ellipticity of the neutron star is ~ 1.17 . The snapshot around the plunge is shown in the lower right panel of Fig. 11. Soon after the onset of the plunge, the two neutron stars contact and the ellipticity is ~ 1.23 . In addition, one can see the appearance of the dynamical tidal lag. It appears even in the absence of viscous dissipation, because the shape of the star cannot follow the rapid change of the tidal potential (see, e.g., Ref. [59]). Therefore, the adiabatic approximation for the tidally induced quadrupole moment determined by Eq. (1) breaks down after the appearance of the dynamical tidal lag. In such a case, the tidal deformability should be evaluated

with the formalism beyond the adiabatic approximation, which is formulated in Ref. [60].

We also note that the ellipticity of the neutron star rapidly increases after the stage at $M\omega = 0.056$. This evolution of the ellipticity is consistent with the semianalytic, Newtonian results [25]. Note that the value of the ellipticity defined here depends on the coordinate system. We here assumed that the coordinate distortion is small because of our choice of the spatial gauge condition.

Finally, we show the difference between the extrapolated gravitational-wave phase and the gravitational-wave phase derived in the PN and EOB approaches for unequal-mass systems APR4-1215 and H4-1215: see Fig. 12. Here, we choose the matching region $(t_1, t_2) = (520M, 1020M)$ for APR4-1215 and $(t_1, t_2) = (600M, 1080M)$ for H4-1215. This figure shows that the feature of the curves for the unequal-mass system is qualitatively the same as those of the equal-mass system, and the magnitude of the phase difference between ϕ_{NR} and $\phi_{\text{PN/EOB}}$ is also as large as that for the equal-mass case.

VI. CONCLUSION

We have explored the property of gravitational waves emitted in the late stage of NS-NS inspirals. To derive the physical waveform from numerical data obtained by NR simulations, we carefully performed the radius and resolution extrapolation of the waveforms. Then, we found the resolution extrapolation is crucial in our present study. Specifically, the accumulated difference between the gravitational-wave phase in the highest grid resolution run and the resolution-extrapolated gravitational-wave phase is ~ 8 radian for APR4 and ~ 3 radian for H4. These values imply that the simulation for the NS-NS inspiral with more compact neutron stars has worse convergence. For the simulation with more compact neutron stars, one needs to perform a higher resolution simulation to derive an accurate waveform. Therefore a sophisticated procedure for the extrapolation is needed to derive an accurate waveform for compact neutron stars. We found that the time-rescaling is a robust prescription for deriving the resolution-extrapolated gravitational-wave phase ϕ_{NR} .

We have compared ϕ_{NR} with $\phi_{\text{PN/EOB}}$, which are derived from the Taylor T4 approximant of the PN formalism and the EOB formalism. Both of the analytic approaches are capable of including the tidal effects. We found that ϕ_{NR} is consistent with $\phi_{\text{PN/EOB}}$ in the early part of the inspiral. On the other hand, in the very late part of the inspiral, ϕ_{NR} evolves more rapidly than $\phi_{\text{PN/EOB}}$. The EOB approach including the tidal corrections up to the next-to-next-to-leading order is currently the best approach for describing the late stage of NS-NS inspirals. However, the estimated accumulated difference between ϕ_{NR} and ϕ_{EOB} is ~ 2.6 radian for APR4, ~ 1.9 radian for H4, and ~ 1.1 radian for MS1 at the moment of contact of the two neutron stars. We

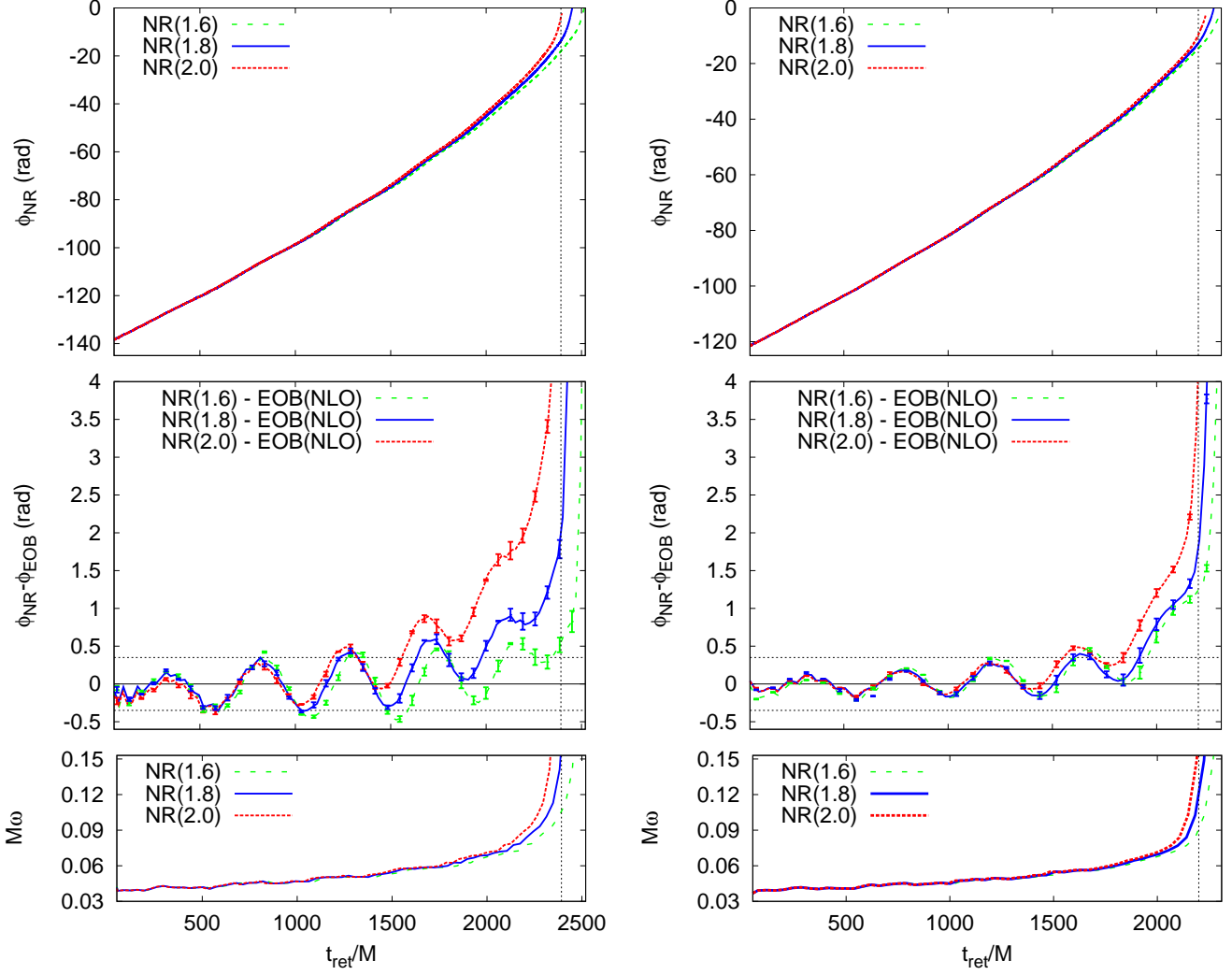


FIG. 6: Gravitational-wave phase (top panels), difference between ϕ_{NR} and ϕ_{EOB} (middle panels), and gravitational-wave angular velocity (bottom panels) for APR4 (left panels) and H4 (right panels). EOB(NLO) denotes the effective-one-body formalism including the tidal effects up to the next-to leading order. We show the curves for the three orders of the convergence, $n = (1.6, 1.8, 2.0)$. The horizontal dashed lines in the middle panels denote the uncertainty due to the modulation of the numerical data. The vertical dashed lines denote the time at contact of the two stars for the case of the order of the convergence is 1.8.

conclude that the tidal effects are still underestimated in the EOB approach including the tidal corrections up to the next-to-next-to-leading order. We also found that this result is independent of the EOS and mass ratio.

Here we make a comparison of our results with the earlier results. We find the absence of the large amplification of the tidal effects in the early inspiral phase suggested in Ref. [30], if the resolution extrapolation is taken into account. In the late inspiral phase, the amplification of the tidal effects is observed. This agrees with the earlier results [30, 34]. In particular, for the MS1 ($C \sim 0.14$), the value of the phase difference between the extrapolated gravitational-wave phase and that of Taylor T4 without

tidal effects is consistent with the results of Ref. [34], which employed the neutron star with $C = 0.14$.

For extracting the tidal deformability of a neutron star efficiently and faithfully from a signal of gravitational waves, one has to prepare a theoretical template of gravitational waves which should be accurate enough up to the onset of the merger. Our present study suggests that the EOB approach including up to the next-to-next-to-leading order tidal correction yields currently the best result. However, for the final orbit, there is still room for the improvement. In the current prescription for incorporating the tidal effects, the adiabatic approximation is assumed for the tidal deformation. For the very close

orbits, however, this approximation breaks down; for example, the presence of the dynamical tidal lag (which is seen in Figs. 10 and 11) cannot be reproduced. If a more sophisticated formalism in which such effects

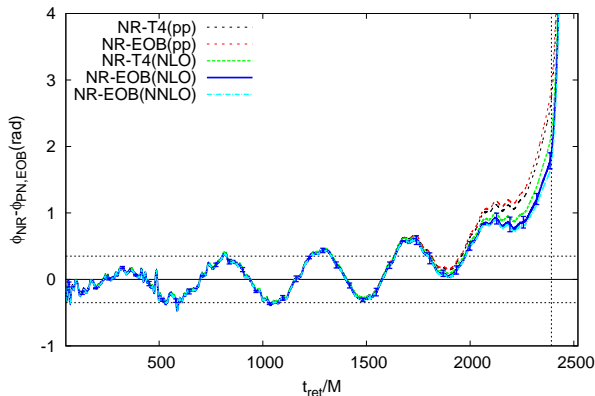


FIG. 7: Phase difference between ϕ_{NR} and $\phi_{\text{PN/EOB}}$ for APR4. In this figure, we set the order of the convergence to be 1.8 for obtaining the extrapolated gravitational-wave phase. T4(pp) and EOB(pp) denote the Taylor T4 approximant and the effective-one-body formalism without the tidal corrections. Here, we only display the error bars of the curve NR-EOB(NLO). However, other curves also have the same amount of the error.

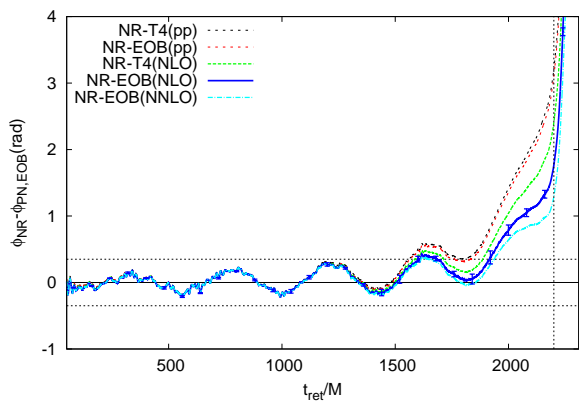


FIG. 8: The same as Fig. 7 but for H4.

are taken in account can be developed, the accuracy of the analytic modeling could be improved (see e.g., Ref [60]).

There is also the issue on the side of numerical relativity. For constructing an analytic model of the gravitational waveform in NS-NS inspirals with a high accuracy, one always calibrates the model waveform by comparing it with the NR result. This implies that a high-accuracy numerical waveform is necessary. To achieve a high accuracy, one needs to perform more accurate simulations than the present ones. One of the keys for improving the accuracy is to reduce the orbital eccentricity in the

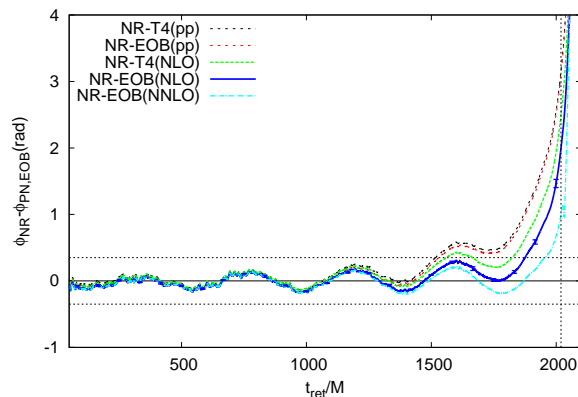


FIG. 9: The same as Fig. 7 but for MS1.

future.

Acknowledgments

We thank A. Buonanno, K. Kiuchi, J. S. Read, and Y. Sekiguchi for useful discussions and comments, and B. D. Lackey and G. Faye for suggesting post-Newtonian and effective one body formalisms for our analysis. This work was supported by Grant-in-Aid for Scientific Research (21340051, 24740163, 21684014), by Grant-in-Aid for Scientific Research on Innovative Area (20105004), by the Grant-in-Aid of JSPS, by HPCI Strategic Program of Japanese MEXT. The work of Hotokezaka is supported by the Grant-in-Aid of JSPS.

-
- [1] B. P. Abbott *et al.*, Rep. Prog. Phys. **72**, 076901 (2009).
 - [2] T. Accadia *et al.*, Class. Quantum Grav. **28**, 025005 (2011).
 - [3] S. Hild, Class. Quantum Grav. **23**, S643 (2006).
 - [4] R. O’Shaughnessy, V. Kalogera, and K. Belczynski, Astrophys. J. **716**, 615 (2010).
 - [5] J. Abadie *et al.*, Class. Quantum Grav. **27**, 173001 (2010).
 - [6] Advanced LIGO, <http://www.advancedligo.mit.edu/>
 - [7] Advanced VIRGO, <http://www.cascina.virgo.infn.it/advirgo/>
 - [8] K. Kuroda: LCGT collaboration, Class. Quantum Grav. **27**, 084004 (2010).
 - [9] C. Cutler, and E. E. Flanagan, Phys. Rev. D **49**, 2658 (1994).
 - [10] M. Shibata, Phys. Rev. Lett. **94**, 201101 (2005).
 - [11] J. S. Read, C. Markakis, M. Shibata, K. Uryu, J. D. E. Creighton, J. L. Friedman, Phys. Rev. D **79**, 124033 (2009).
 - [12] K. Kiuchi, Y. Sekiguchi, M. Shibata, and K. Taniguchi, Phys. Rev. Lett. **104**, 141101 (2010).

- [13] Y. Sekiguchi, K. Kiuchi, K. Kyutoku, and M. Shibata, *Phys. Rev. Lett.* **107**, 211101 (2011).
- [14] N. Andersson, V. Ferrari, D. I. Jones, K. D. Kokkotas, B. Krishnan, J. S. Read, L. Rezzolla, and B. Zink, *Gen. Rel. Grav.* **43**, 409A, (2011).
- [15] B. D. Lackey, K. Kyutoku, M. Shibata, P. R. Brady, and J. L. Friedman, *Phys. Rev D* **85**, 044061 (2012).
- [16] A. Bauswein and H. -T. Janka, *Phys. Rev. Lett.* **108**, 011101 (2012).
- [17] A. Bauswein, H. -T. Janka, K. Hebeler, and A. Schwenk, *Phys. Rev. D* **86**, 063001 (2012).
- [18] T. Mora, and C. M. Will, *Phys. Rev. D* **69**, 104021 (2004).
- [19] C. Messenger and J. Read, *Phys. Rev. Lett.* **108**, 091101 (2012).
- [20] Punturo, *et al.*, *Class. Quantum Grav.* **27**, 194002 (2010).
- [21] E. E. Flanagan, and T. Hinderer, *Phys. Rev. D* **77**, 021502(R) (2008).
- [22] T. Hinderer, B. D. Lackey, R. N. Lang, and J. S. Read, *Phys. Rev. D* **81**, 123016 (2010).
- [23] T. Damour, A. Nagar, and L. Villain, *Phys. Rev. D* **85**, 123007 (2012).
- [24] P. B. Demorest, T. Pennucci, S. M. Ransom, M. S. E. Roberts, and J. W. T. Hessels, *Nature* **467**, 1081 (2010).
- [25] D. Lai, F. A. Rasio, and S. L. Shapiro, *Astrophys. J.* **420**, 811 (1994).
- [26] D. Bini, T. Damour, and G. Faye, *Phys. Rev. D* **85**, 124034 (2012).
- [27] M. D. Duez, *Class. Quantum Grav.* **27**, 114002 (2010).
- [28] M. Shibata and K. Taniguchi, *Living Rev. Relativ.* **14**, 6 (2011).
- [29] J. A. Faber and F. A. Rasio, *Living Rev. Relativ.* **15**, 8 (2012).
- [30] L. Baiotti, T. Damour, B. Giacomazzo, A. Nagar, and L. Rezzolla, *Phys. Rev. D* **84**, 024017 (2011).
- [31] M. Thierfelder, S. Bernuzzi, and B. Brügmann, *Phys. Rev. D* **84**, 044012 (2011).
- [32] K. Hotokezaka, K. Kyutoku, H. Okawa, M. Shibata, and K. Kiuchi, *Phys. Rev. D* **83**, 124008 (2011).
- [33] L. Baiotti, T. Damour, B. Giacomazzo, A. Nagar, and L. Rezzolla, *Phys. Lett.* **105**, 0261101 (2010).
- [34] S. Bernuzzi, M. Thierfelder, and B. Brügmann, *Phys. Rev. D* **85**, 104030 (2012).
- [35] S. Bernuzzi, A. Nagar, M. Thierfelder, and B. Brügmann, *Phys. Rev. D* **86**, 044030 (2012).
- [36] J. S. Read, B. D. Lackey, B. J. Owen, and J. L. Friedman, *Phys. Rev. D* **79**, 124032 (2009).
- [37] T. Hinderer, *Astrophys. J.* **677**, 1216 (2008).
- [38] T. Damour, and A. Nagar, *Phys. Rev. D* **80**, 084035 (2009).
- [39] T. Binnington, and E. Poisson, *Phys. Rev. D* **80**, 084018 (2009).
- [40] J. Vines, E. E. Flanagan, and T. Hinderer, *Phys. Rev. D* **83**, 084051 (2011).
- [41] M. Boyle, D. A. Brown, L. E. Kidder, A. H. Mroue, H. P. Pfeiffer, M. A. Scheel, G. B. Cook, and S. A. Teukolsky, *Phys. Rev. D* **76**, 124038 (2007).
- [42] T. Damour and A. Nagar, *Phys. Rev. D* **81**, 084016 (2010).
- [43] A. Buonanno and T. Damour, *Phys. Rev. D* **59**, 084006 (1999).
- [44] A. Buonanno and T. Damour, *Phys. Rev. D* **62**, 064015 (2000).
- [45] T. Damour, *Phys. Rev. D* **64**, 124013 (2001).
- [46] Y. Pan, A. Buonanno, M. Boyle, L. T. Buchman, L. E. Kidder, H. P. Pfeiffer, and M. A. Scheel, *Phys. Rev. D* **84**, 124052 (2011).
- [47] T. Yamamoto, M. Shibata, and K. Taniguchi, *Phys. Rev. D* **78**, 064054 (2008).
- [48] M. Shibata and T. Nakamura, *Phys. Rev. D* **52**, 5428 (1995).
- [49] T. W. Baumgarte and S. L. Shapiro, *Phys. Rev. D* **59**, 024007 (1998).
- [50] M. Campanelli, C. O. Lousto, P. Marronetti, and Y. Zlochower, *Phys. Rev. Lett.* **96**, 111101 (2006); J. G. Baker, J. Centrella, D.-I. Choi, M. Koppitz, and J. van Meter, *Phys. Rev. Lett.* **96**, 111102 (2006); L. Baiotti, M. Shibata, and T. Yamamoto *Phys. Rev. D* **82**, 064015 (2010).
- [51] B. Brügmann, J. A. Gonzalez, M. Hannam, S. Husa, U. Sperhake, and W. Tichy, *Phys. Rev. D* **77**, 024027 (2008).
- [52] A. Kurganov and E. Tadmor, *J. Comput. Phys.* **160**, 241 (2000).
- [53] LORENE webpage: <http://www.lorene.obspm.fr/>
- [54] L. Bildsten, and C. Cutler, *Astrophys. J.* **400**, 175 (1992).
- [55] C. S. Kochanek, *Astrophys. J.* **398**, 234 (1992).
- [56] A. Akmal, V. R. Pandharipande, and D. G. Ravenhall, *Phys. Rev. C* **58**, 1804 (1998).
- [57] N. K. Glendenning and S. A. Moszkowski, *Phys. Rev. Lett.* **67**, 2414 (1991).
- [58] A. J. Penner, N. Andersson, L. Samuelsson, I. Hawke, and D. I. Jones, *Phys. Rev. D* **84**, 103006 (2011).
- [59] D. Lai, *Mon. Not. R. Astron. Soc.*, **270**, 611 (1994).
- [60] V. Ferrari, L. Gualtieri, and A. Maselli, *Phys. Rev. D* **85**, 044045 (2012).

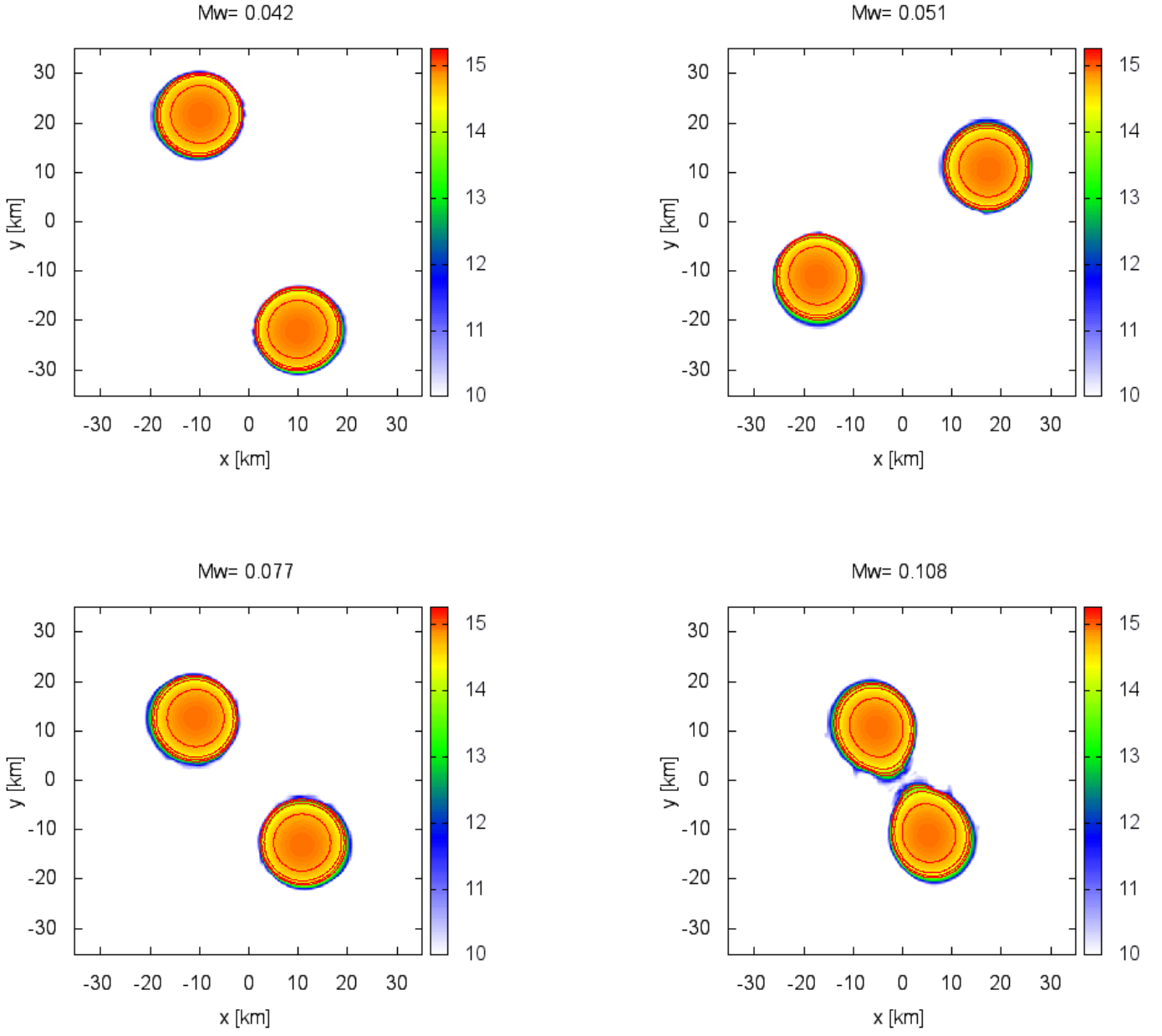


FIG. 10: Snapshots of the orbital-plane density profile of NS-NS binaries in close orbits for APR4. The color denotes the density in units of $\log \rho$ (g/cm^3).

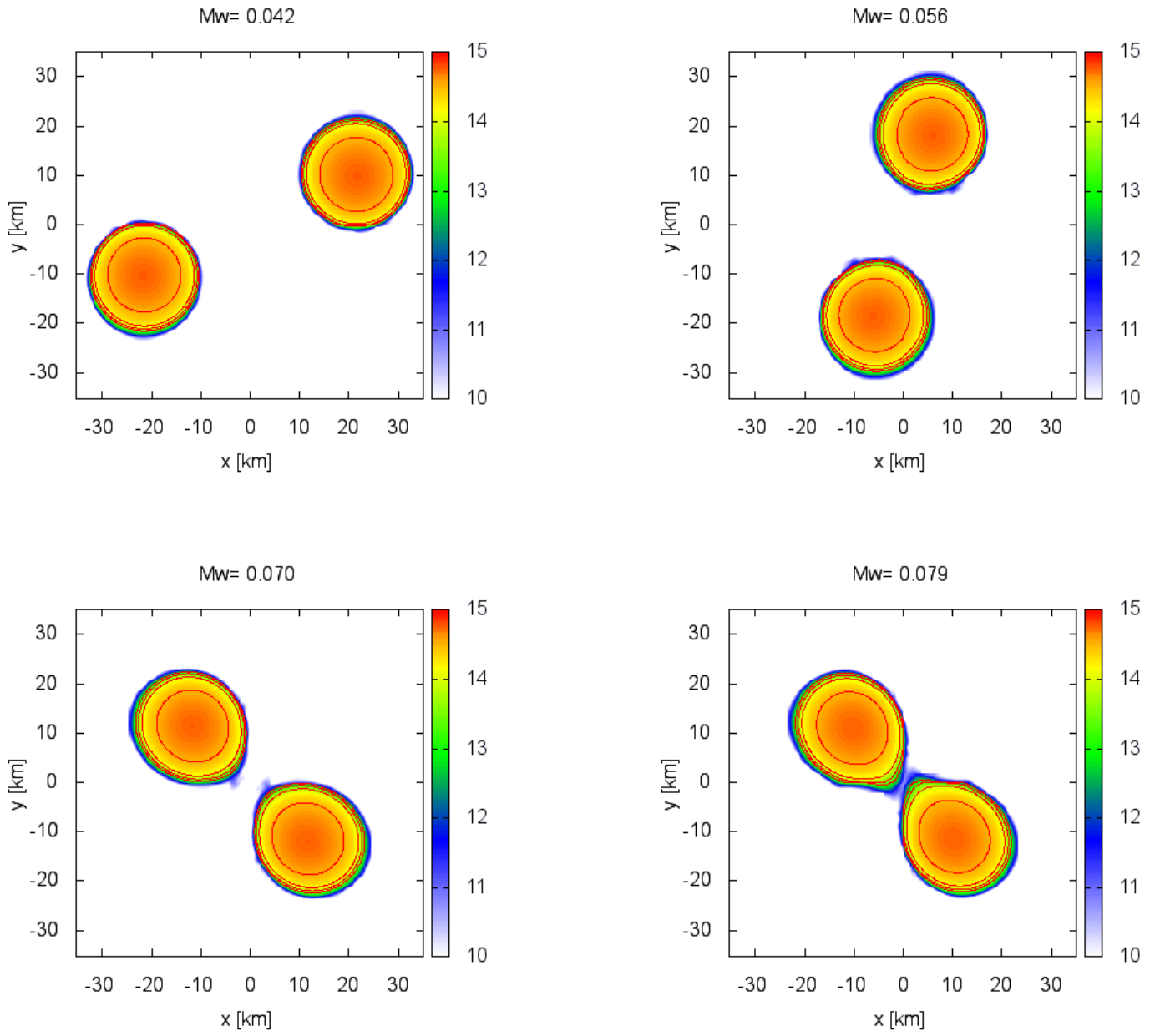


FIG. 11: The same as Fig.10 but for H4.

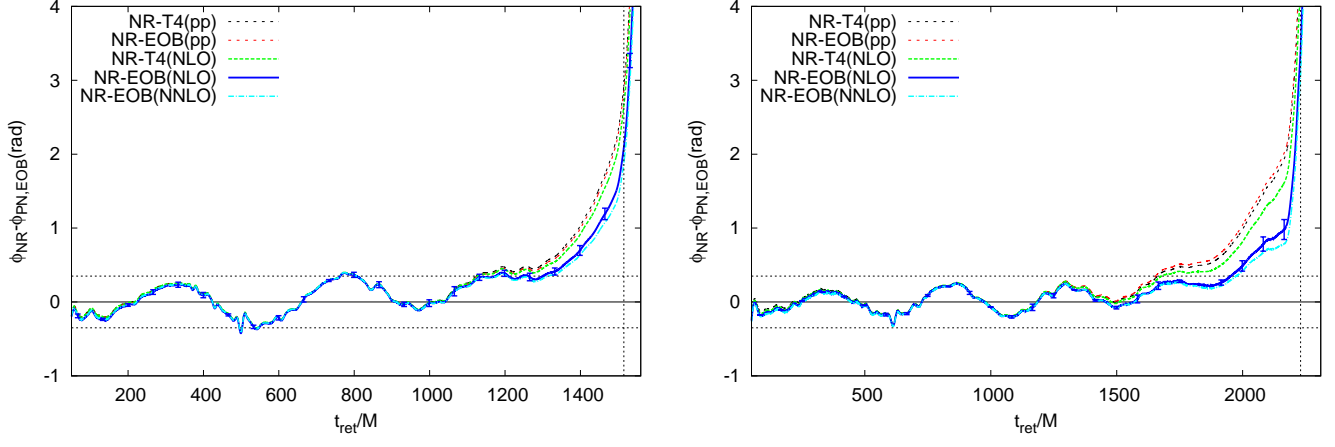


FIG. 12: Difference between ϕ_{NR} and $\phi_{\text{PN/EOB}}$ for APR4-1215 (left panel) and for H4-1215 (right panel). Here we choose $n = 1.8$.